Sardinia Radio Telescope structural behavior under solar thermal load

Alessandro Attoli
alessandro.attoli@inaf.it, INAF–OAC Osservatorio Astronomico di Cagliari, Selargius, Italy

Flavio Stochino*
Corresponding Author: fstochino@unica.it, DICAAR, Università degli Studi di Cagliari, via Marengo 2, 09123 Cagliari, Italy

Franco Buffa
franco.buffa@inaf.it, INAF–OAC Osservatorio Astronomico di Cagliari, Selargius, Italy

Sergio Poppi
sergio.poppi@inaf.it, INAF–OAC Osservatorio Astronomico di Cagliari, Selargius, Italy

Giampaolo Serra
giampaolo.serra@asi.it, Agenzia Spaziale Italiana (ASI), CSG-Unità Capo Sito Sardegna, Sede ASI-Cagliari, presso INAF–OAC Osservatorio Astronomico di Cagliari, Selargius, Italy

Giannina Sanna
topoca@unica.it, DICAAR, Università degli Studi di Cagliari, via Marengo 2, 09123 Cagliari, Italy

Antonio Cazzani
antonio.cazzani@unica.it, DICAAR, Università degli Studi di Cagliari, via Marengo 2, 09123 Cagliari, Italy

Abstract

Sardinia Radio Telescope (SRT) with its 64m diameter primary mirror is a modern radio-astronomic facility. Its large dimensions allow to reach high performances, but, at the same time, make the antenna sensitive to deformations caused by environmental factors such as gravity, wind and temperature changes. Indeed, it is important to determine the effects that environmental loads produce on this structure. In this paper, the SRT pointing error variation produced by solar radiation acting on its structural system has been studied. Through a sensitivity analysis it was possible to establish that the Alidade is the radio telescope component that produces higher pointing errors when subjected to thermal load. Then, an analytical model was used to estimate the temperature of the Alidade trusses exposed to solar radiation. Furthermore, the calibration of the analytical model parameters was performed by comparing the experimental data obtained by thermographic

Please cite this document as: Attoli, A., Stochino, F., Buffa, F., Poppi, S., Serra, G., Sanna, G., & Cazzani, A. (2022). Sardinia Radio Telescope structural behavior under solar thermal load. In *Structures*, 39: 901-916. DOI: 10.1016/j.istruc.2022.03.065

investigations. Then, using Finite Element Analysis, the pointing error generated by each simulated thermal scenario was determined. Finally, the numerical results allow to better understand the structural behavior of SRT in realistic thermal conditions.

1. Introduction

Protected from urban electromagnetic interference, not too far from Cagliari (Italy), the Sardinia Radio Telescope (SRT – www.srt.inaf.it) scans the sky. With its 64m diameter primary mirror, SRT is a modern radio-astronomic facility. It has a Gregorian configuration, with a shaped primary mirror (M1) and an elliptical shaped secondary mirror (M2). The main mirror is characterized by an active surface made up of panels that can be oriented by means of electromechanical actuators, (Bolli et al., 2015), (Stochino et al., 2015), (Buffa et al., 2015). SRT has been designed to work inside a frequency band between 300MHz and 116GHz (wavelength range between 1000 mm and 3 mm).

Its large aperture allows to reach high antenna gain and formidable angular resolution. Generally, this kind of antenna has the best performances in small elevation angular ranges around the elevation at which its mechanical alignment has been done (at 45 deg in the case of SRT). At other angular elevations, i.e. varying the pointing direction of the antenna, the performances get worse, if not compensated, decreasing the gain and the pointing accuracy. This is due to the gravitational loads, which mainly change the profile of the main reflector surface and modify the alignment between main and sub-reflectors, to the thermal load and to the wind pressure, which can deform the beam structure (alidade) supporting the reflectors and modify the main reflectors positions. The SRT active optics can compensate the main reflector deformations and the reflectors axis alignment by dedicated look-up tables coming from photogrammetry and laser tracker combined measurements (Süss et al., 2012). Instead, the effect of the thermal loads and the wind on the SRT pointing accuracy needs a deep investigation, now more than ever, considering that the antenna is about to be upgraded with higher frequency receivers which will allow to extend the maximum operative frequency from 26.5 GHz (required pointing accuracy 4.4 arcsec) to 116 GHz (required pointing accuracy 1 arcsec) (Govoni et al., 2021). Therefore, it would be important to optimize the position of thermal sensors after a sensitivity study on what are the most SRT parts that mostly influence the pointing error due to thermal deformations.

In literature, the non-uniform thermal load has been analyzed for many complex three-dimensional structures (Chen et al., 2020), (Chen et al., 2021) considering also the fatigue effects caused by cyclic thermal loads (Wang at al., 2021).

If we focus on telescopes, the great influence of the alidade on pointing error has been already highlighted in many cases. In (Fu et al., 2016) the effects on pointing accuracy due to real temperature field distributions on the TM65m antenna alidade were analyzed; thermal deformations were computed from measures taken by inclinometers. (Ambrosini et al., 2016) describes how the thermal behavior of the of the 32 meter VLBI parabola at Medicina was studied, through the data collected with thermal sensors distributed on the alidade and an inclinometer positioned in the axis of elevation.

How to use inclinometer information for monitoring the rail and the thermal gradient effects on the SRT Alidade structure is presented in (Pisanu et al., 2014). (Ukita et al., 2007) also propose a study of the effects that thermal loads together with wind action produce on the ASTE 10-m Antenna.

In order to determine the thermal load due to solar radiation it is possible to use a numerical approach, based on computational fluid dynamics (Drozdzol, 2021), (Losi et al., 2021), or to develop an experimental campaign measuring real temperatures on site (Li et al., 2021). In the latter paper the problem is treated through an approach based on Finite Element (FE) method integrated with field measurements that allow to develop a model updating capable of reaching good accuracy. An example is proposed in (Zhao et al., 2019) in which the FE method is used to study of the effects on the pointing of radio telescopes caused by gravity, thermal gradients, and wind disturbances. In (Greve et al., 2005), temperature measurements are applied to finite element model in order to calculate structural deformation of the Institut de Radioastronomie Millimétrique 30-m telescope.

(Stochino et al., 2015) describe a method for updating a finite element model of the Sardinia Radio Telescope in order to more accurately estimate the displacements of the structure caused by gravity and thermal loads. The latter approach uses the photogrammetric survey as the only benchmark. (Buffa et al., 2015) presents the results of Finite Element analyses to make a comparison with the experimental data deriving from photogrammetric investigations.

The evaluation of the correlation of antennas pointing error and solar thermal load is a current research topic that requires further investigations. In addition, given that SRT will be upgraded soon with higher frequency receivers the accurate evaluation of thermal loads effects is of paramount relevance. Thus, this paper investigates the antenna pointing error produced by solar radiation, taking into account possible phenomena of differentiated irradiation due to shading and exposure using innovative analytical and numerical models.

After this brief introduction, in Section 2, a sensitivity analysis is proposed to identify the components of the telescope that most influence pointing under thermal load. The study of the effects on pointing generated by a uniform thermal load scenario is described in Section 3. Section 4 is dedicated to the presentation of an analytical model for estimating the temperature of a surface subjected to solar radiation. A methodology to estimate radiation using commercial software is presented in Section 5. Section 6 proposes a method to calibrate, through thermographic investigations, the parameters that modify heat balance. The numerical results of the Finite Element Analyses (FEA) are described in Section 7. Finally, concluding remarks and future developments are drawn in Section 8.

2. Pointing error sensitivity analysis

At first, it is necessary to define a parameter that clearly indicates the direction observed by Sardinia Radio Telescope when it receives the signal from a source in the sky. At the same time, this parameter must provide information on the accuracy of the observations and on possible pointing errors.

For this reason, an ideal vector located in the intersection between azimuth and elevation axes (Figure 1), which in the absence of any load has an ideal direction, represents the reference parameter for estimating the pointing error. For the sake of clarity: the elevation angle is equal to zero when the pointing vector lies on a horizontal plane and it is equal to 90 deg when the pointing vector coincides with the alidade rotation axis.

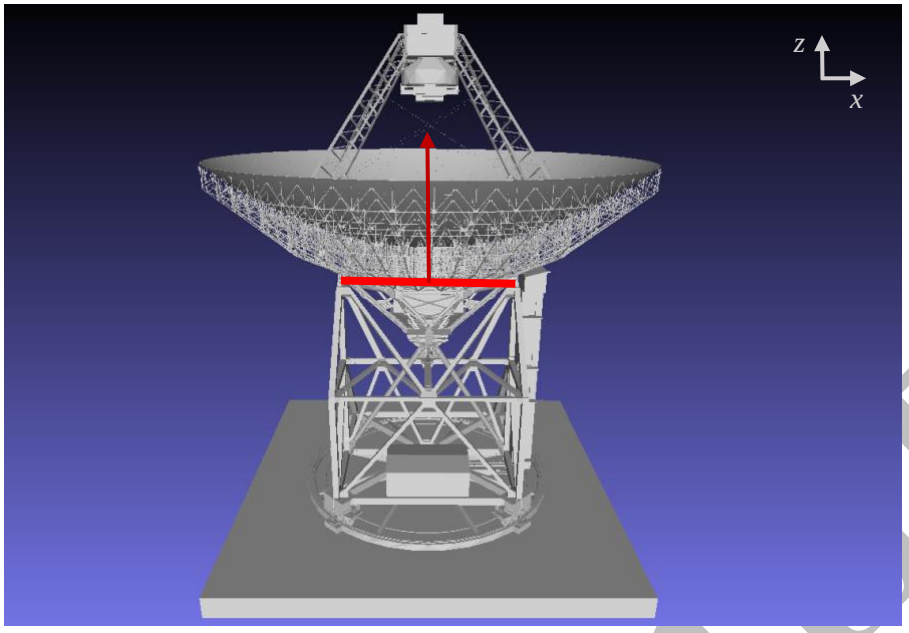

Figure 1: Theoretical pointing vector of SRT when the antenna is at an elevation angle of 90 deg.

This vector direction changes with the variation of the parabola elevation and the alidade rotation around the vertical axis. The definition of the pointing vector does not consider the effects of M2 positioned in the quadrupod peak. At this moment, also thermal loads are not considered and the current corrections are based only on a metrological system.

Due to external actions, the SRT pointing vector undergoes rotations and translations with respect to its ideal position. However, given that the observed objects are located at infinite distance from the observer, the translations don't affect the pointing error. Instead, small rotations can lead to large errors in pointing an astronomical target. In order to identify which components of the radio telescope have the greatest influence on focus pointing when subjected to thermal stress, a sensitivity analysis was performed using a finite element model of SRT developed in ANSYS environment (Stolarski et al., 2018).

The ANSYS finite element (FE) model of the antenna is composed of 93,635 elements and 92,788 nodes; the presented composition of the 3D system produced a total amount of degrees of freedom equal to 463,871 (Figure 2).

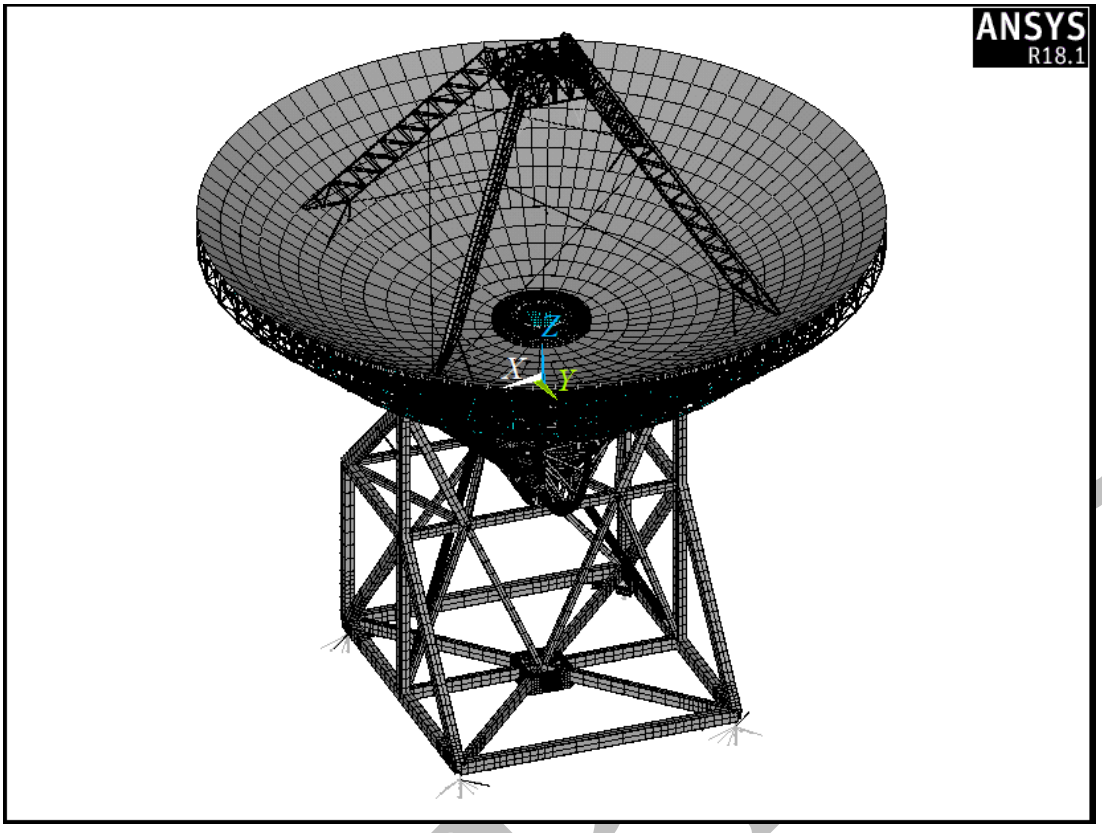

Figure 2: Finite Element Model of the Sardinia Radio Telescope at an elevation angle of 90°.

The cartesian reference axes *x,y,z* are presented in Figure 2, while the rotation axis points the rotations around the azimuth or vertical direction (that coincides with *z* axis in Figure 2) and the elevation axis define the rotations in the plane containing the azimuth and the horizontal direction.

The parts that can be recognized in the described model are listed in the following bottom-up sequence:

- *Reinforced concrete base and foundation rail:* although they have not been modelled, they are considered through appropriate constraints at the base to ensure the verticality of the azimuth axis;
- *Alidade:* structural frame that supports all the moving components that can tilt around the elevation axis; it is modelled using both two-noded Timoshenko beam elements with seven degrees of freedom per node (linear translations along the *x*- ,*y*-, *z*-direction, rotations around the *x*- ,*y*-, *z*-axis, and warping), and two-noded beam elements with six degrees of freedom per node (linear translations along the *x*- ,*y*-, *z*-direction and rotations around the *x*- ,*y*-, *z*-axis).
- *Back Up Structure (BUS*): Truss structure which supports the primary mirror, connected to the alidade through the cradle containing the elevation axis; it is modeled by assembling two-noded beam elements

with six degrees of freedom per node (linear translations along the x- ,y-, z-direction and rotations around the x- ,y-, z-axis) in order to obtain a refined 3D system.

- *Primary Mirror (M1):* active surface with a diameter of 64m composed of 1008 aluminium panels which can be moved by 1116 electromechanical actuators; Each panel is modeled by means of a four-noded shell element with six degrees of freedom per node (linear translations along the x- ,y-, z-direction and rotations around the x- ,y-, z-axis) and it is connected to the BUS by means of rigid multi-point-constraint element.
- *Quadrupod structure:* four legs truss structure that support the Secondary Mirror (M2) and the Prime Focus Positioner (PFP) which hosts some receivers; it is modelled using two-noded Timoshenko beam elements and four-noded shell elements; both have six degrees of freedom per node (linear translations along the x- ,y-, z-direction and rotations around the x- ,y-, z-axis).
- *Secondary Mirror (M2):* secondary reflector positioned on the top of the Quadrupod structure. Only the support structures of the component were modeled, through multi-point-constraint elements; lumped mass elements complete the representation of M2.

A summary of the number of elements and nodes that make up each part of the Finite Element Model is presented in Table 1.

Macro-components	Number of Elements	Number of Nodes
Alidade	4389	4234
Cradle	13187	14721
Back Up Structure	60256	61982
Primary Mirror	1008	1104
Quadrupod	2888	3254
Secondary Mirror	24	16

Table 1 : Number of Elements and Nodes which each macro-component of Sardinia Radio Telescope's FE model is composed

The Alidade is symmetrical with respect to the *z-y* plane, see Figure 2, while no symmetries can be found in the *z-x* plane.

The components with a structural role (Alidade, BUS and Quadrupod), have been modelled assuming that they are made of isotropic steel with density μ_s = 7908.5 kg/m^3, Young's modulus E_s = 199.95 GPa and Poisson's ratio ν_s = 0.29. Its linear thermal expansion coefficient ψ_s is equal to 1.17×10^{-5} ◦C^{-1}. Overall, the FE model presents a total weight of 31.730 MN.

Therefore, in this work the effects produced by thermal loads have been described with the Pointing Vector Rotation (PVR) parameter; it is expressed by Eq. (1):

$$\mathrm{PVR} = \sqrt{(\varphi_x)^2 + \left(\varphi_y\right)^2 + (\varphi_z)^2} \quad (1)$$

in which φ_x, φ_y and φ_z are the rotations of the pointing vector with respect to the ideal direction. They should be zero in the ideal condition, while their values change as the pointing vector differs from the ideal position. Given that the model is developed in a linear elasticity framework we can enforce the principle of overlapping effects using an iterative approach. Indeed, by iteratively applying a thermal load of 10 ° C to each element of the FE, it was possible to identify which one have the greatest impact on the pointing vector. The thermal gradient produces a thermal expansion of the considered element. Relating the value of the pointing error to the element subjected to the thermal gradient yields to an element importance rank.

To simplify the problem, the Sardinia Radio Telescope has been divided into four macro-components (Alidade, Cradle, Back Up Structure, Quadrupod) which are separately shown in the Figure 3:

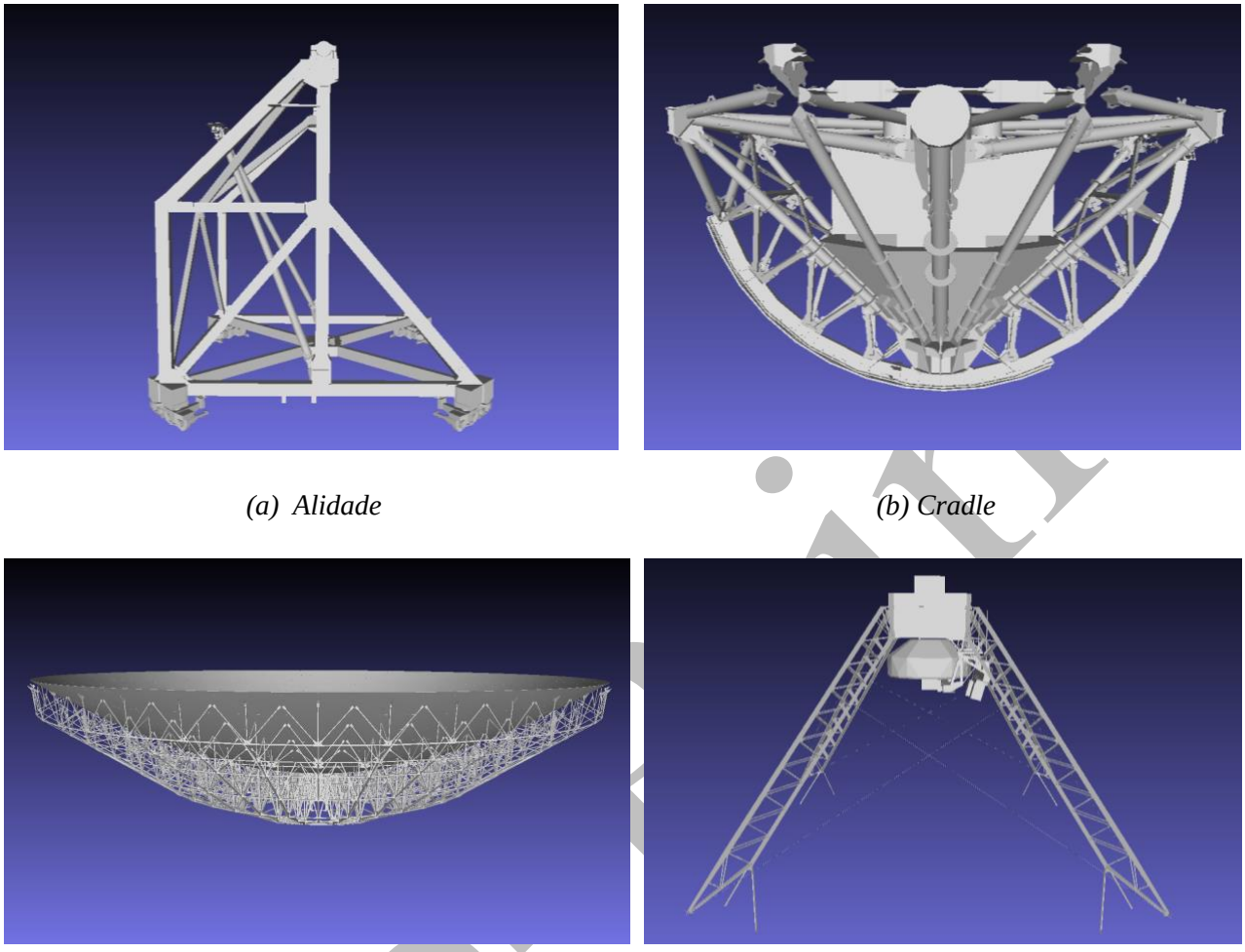

(a) Alidade *(b) Cradle*

(c) Back Up Structure *(d) Quadrupod*

Figure 3: SRT macro-components used for pointing error element ranking.

Figures 4-7 present the pointing error control parameter expressed in arcseconds, for each of the macro-components analyzed with SRT at *90* deg elevation.

Looking at Figure 4 it is important to clarify that each point represents the element barycenter, while the elevator has been represented by a set of point mass and for this reason some truss present more colour points than others. Boundary conditions are represented by the solid basement model and by a set of kinematic relationships between displacements and rotations on the rail base circle.

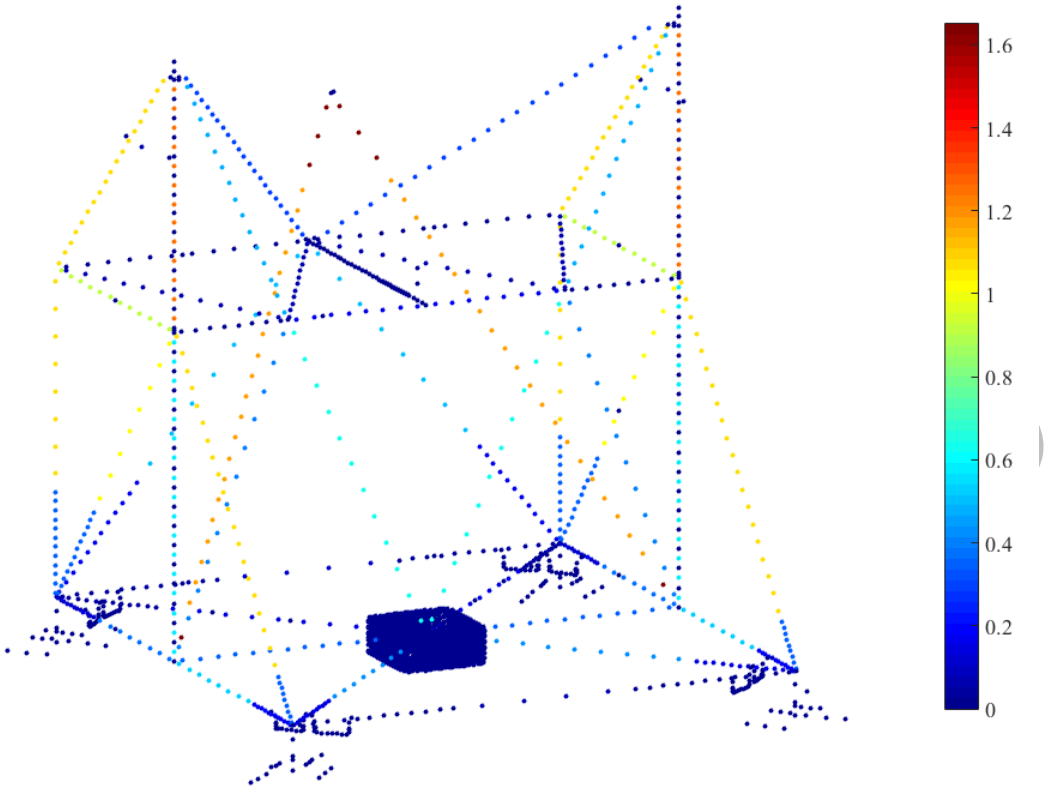

Figure 4: Pointing Vector Rotation (in arcsec) for the Alidade's elements. Representation referred to 90 deg elevation.

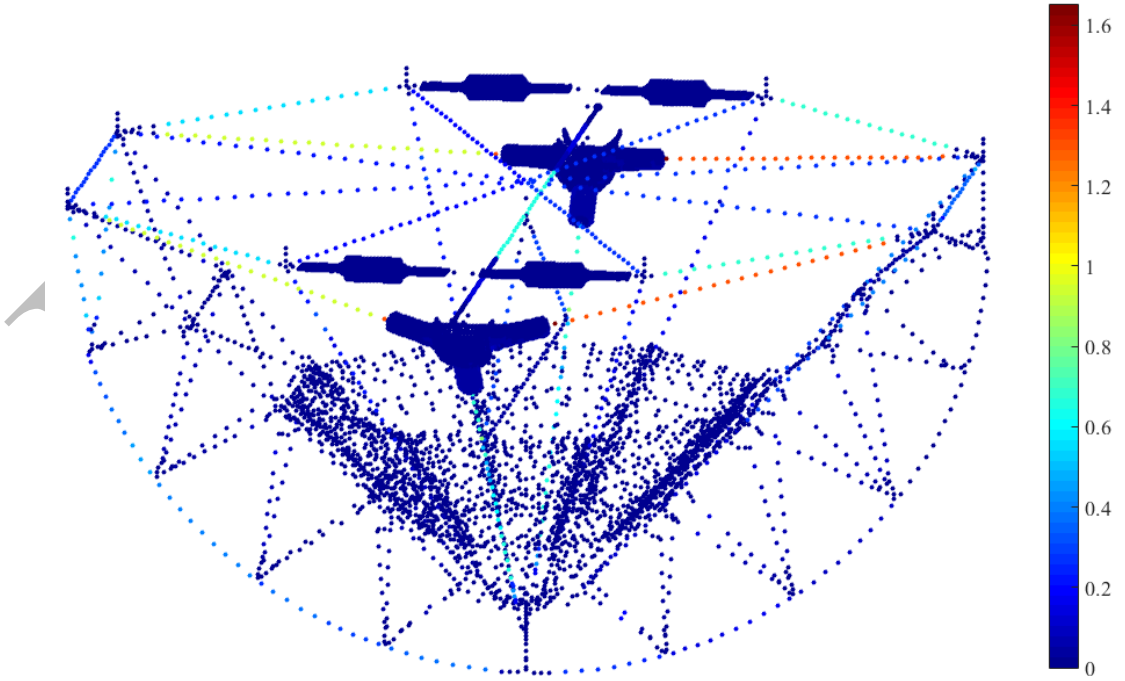

Figure 5: Pointing Vector Rotation (in arcsec) for the Cradle's elements. Representation referred to 90 deg elevation.

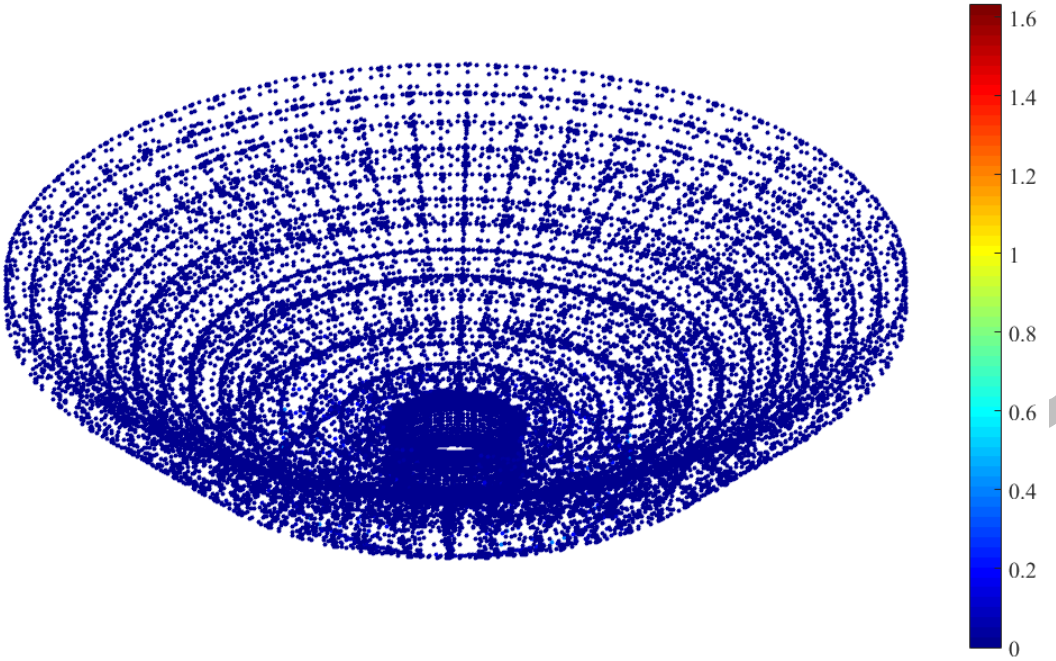

Figure 6: Pointing Vector Rotation (in arcsec) for BUS's elements. Representation referred to 90 deg elevation.

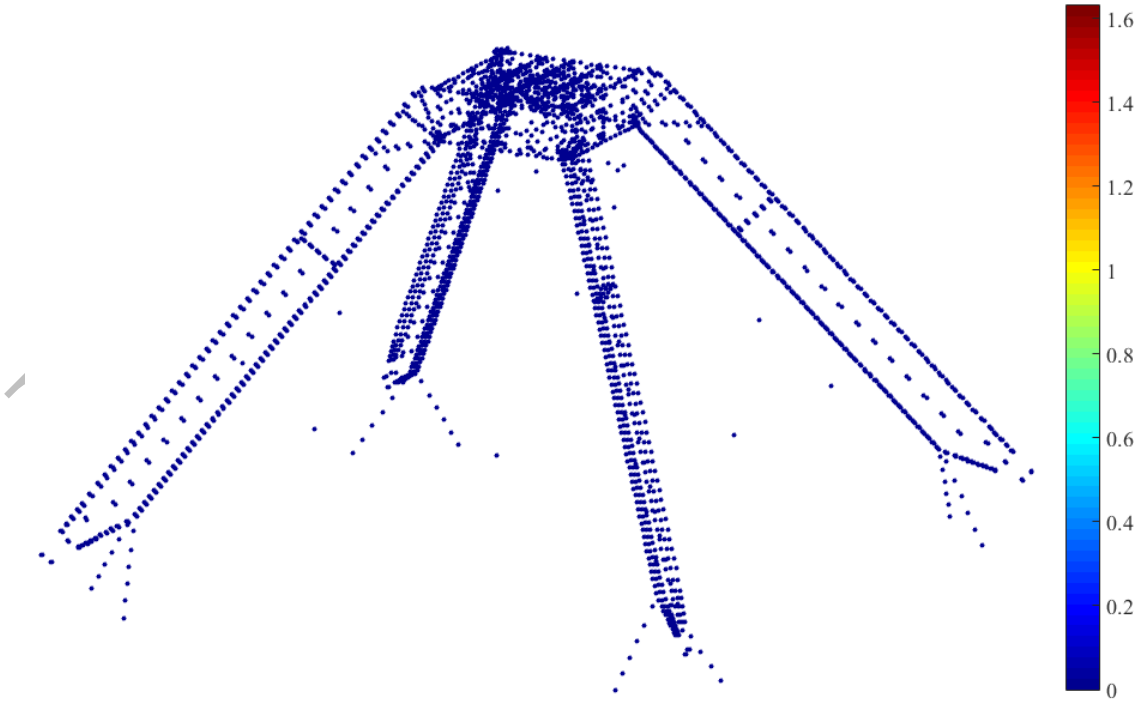

Figure 7: Pointing Vector Rotation (in arcsec) for the Quadrupod's elements. Representation referred to 90 deg elevation

The results presented by Figures 4-7 show that the alidade produces the greatest pointing errors in case of thermal load. Furthermore, the contribution offered by the Cradle should not be overlooked. Minor influence is instead produced by Back Up Structure and Quadrupod.

Therefore, these results suggest that the Alidade is the component of the radio telescope on which it is appropriate to focus more attention in this study, and provide an element ranking for pointing error produced by the thermal load. This aspect is of particular interest when it is necessary to identify the most suitable position to install thermal sensors.

Other sensitivity analyses, not reported here for the sake of synthesis, showed that different elevation angles (90 deg, 60 deg and 30 deg) present similar results.

3. Pointing Vector Rotation for uniform temperature distribution

In this section the rotation of the pointing vector has been studied in case of uniform temperature distributions in the 49 trusses of the Alidade. Studying this condition allows us to analyse the behavior of the structure under a uniform thermal load, neglecting the effects of shading and considering only geometrical and thermo-mechanical characteristics.

Three load cases were analyzed with 90 deg antenna elevation and the uniform temperature gradient equal to 5°C, 10°C and 15°C. The values of the components that generate the total rotation of the pointing vector are reported in Table 2. As already presented in the introduction the SRT minimum resolution at maximum frequency is 1 arcsec. The small values of φ_y and φ_z can be explained considering the numerical errors of the model.

T [°C]	φ_x [arcsec]	φ_y [arcsec]	φ_z [arcsec]
5	0.32542	0.00052	0.01248
10	0.65087	0.00104	0.02496
15	0.97629	0.00156	0.03743

Table 2 : Rotation components of the Point vector for different uniform temperature distributions (5 – 10 – 15 [°C]) .

The numerical values shown in the Table 2 indicate that the rotation around the *x*-axis is predominant over the others in all three analyzed cases: two orders of magnitude with respect to φ_y and one order of magnitude with respect to φ_z. This is due to the structural symmetry of the Alidade. Actually, symmetrical elements produce rotations around the *x*-axis with the same direction, while the rotations around the *y* and *z* axes are both discordant; thus, φ_y and φ_z tend to cancel out each other in the case of uniform thermal load in symmetric trusses. The rotation around the elevation axis (*x*-axis) is instead linked to the temperature difference between the trusses that produce positive φ_x and negative φ_x and is therefore independent of the structural symmetry with respect to the z-*y* plane of the Alidade. In addition, it is important to remember that no-symmetry is present with respect to the z-x plane.

In order to evaluate what has been described in a qualitative way, it is necessary to introduce a coefficient of influence that takes into account the effects on the pointing vector produced by each element when subjected to positive thermal load. This is necessary to obtain weighted temperatures for the trusses, preventing temperatures applied to elements that produce important positive rotations from being cancelled out by temperatures applied to trusses that instead produce opposite effects that produce smaller pointing errors.

We introduce the Influence Coefficients (IC) for the three rotation components for each of the 49 trusses. These IC are obtained by dividing the rotation component of the pointing vector produced by each element with respect to the maximum value found for the same rotation component.

The Weighted Temperature is estimated by multiplying the temperature applied to each element by the respective IC.

The algebraic sum of the weighted temperatures defines the total thermal gradient among the set of trusses that produce positive rotations and those that produce negative rotations (2).

$$\mathrm{WTG}_i = \sum_{j=1}^{49} \mathrm{IC}_{ij} \quad T_j \tag{2}$$

Eq. (2) expresses the Weighted Thermal Gradient for the *i*-th rotation component ($i = x, y, z$), in which the subscript *j* indicates the numerical labels of the trusses (see Figure 8).

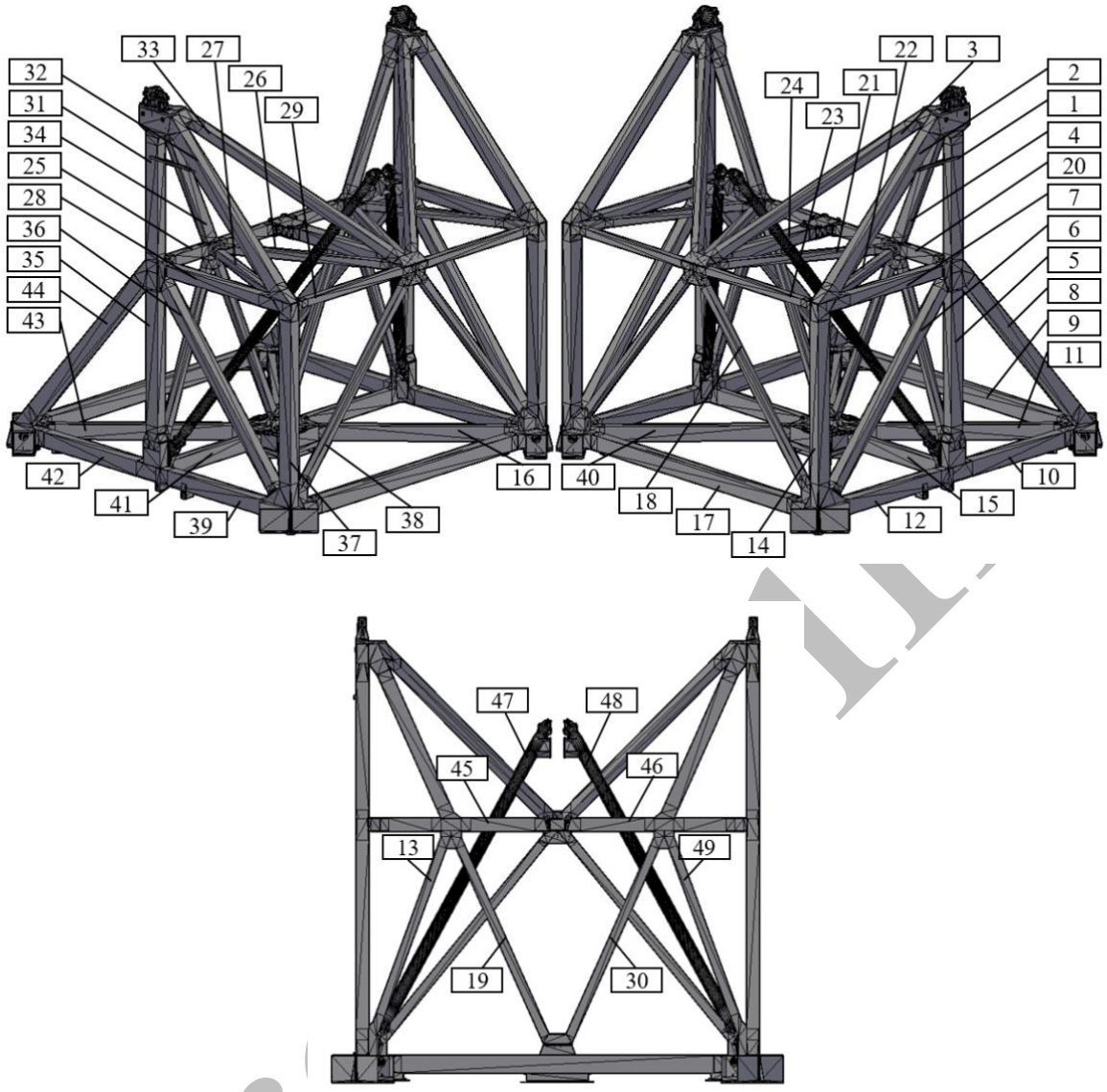

Figure 8: Numerical coding of the Alidade's trusses.

Figure 9 shows the values of the IC referred to each Alidade truss element, and for each rotation component (φ_x, φ_y and φ_z): the color of each point represents the truss IC value of which is part. Figures 10-12, which are referred respectively to *x*, *y* and *z* rotation components, shows the Weighted temperature for all uniform temperature distributions analyzed (5 – 10 – 15 [°C]):): the color of each point represents the truss Weighted temperature value of which is part. Moreover Table 3 presents the values of the WTG for each rotation component, which are produced by the three uniform temperature distributions considered.

It can be noted that the WTG referred to the rotation around the *x*-axis is higher than the one that produce rotations around the *y* and *z* axes, this can be explained with the effects of geometric symmetry described above.

With reference to the rotation around the *x*-axis, there is an upward trend of the WTG with the increase in temperature applied to the trusses, which justifies the increase in the total rotation of the pointing vector.

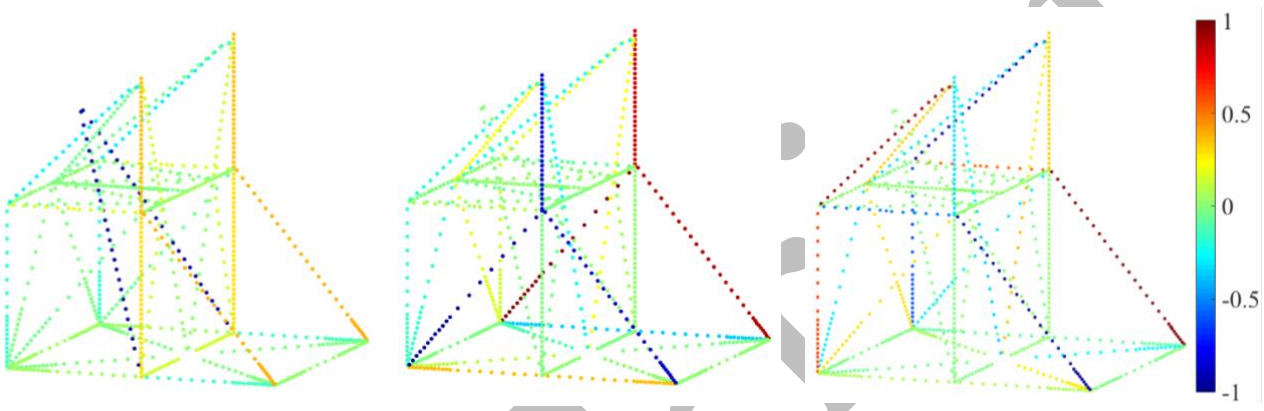

(a) φ_x *component* *(b)* φ_y *component* *(c)* φ_z *component*

Figure 9: Values of the Influence Coefficient (IC) *on the pointing produced by alidade truss elements, for each rotation component (* φ_x, φ_y *and* φ_z *).*

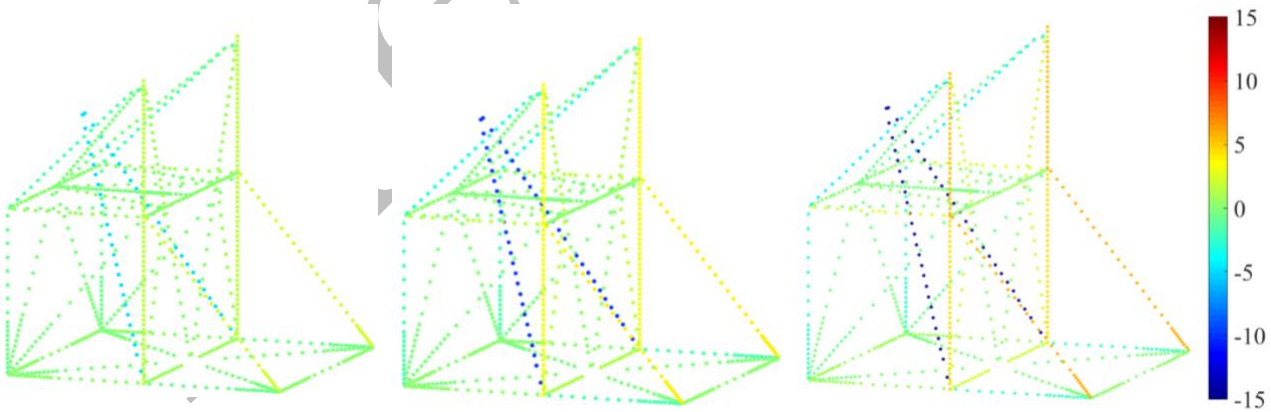

(a) $T = 5\ °C$ *(b)* $T = 10\ °C$ *(c)* $T = 15\ °C$

Figure 10: Weighted temperature for different uniform temperature distributions (5 – 10 – 15 [°C]) – φ_x *component.*

Please cite this document as: Attoli, A., Stochino, F., Buffa, F., Poppi, S., Serra, G., Sanna, G., & Cazzani, A. (2022). Sardinia Radio Telescope structural behavior under solar thermal load. In *Structures*, 39: 901-916. DOI: 10.1016/j.istruc.2022.03.065

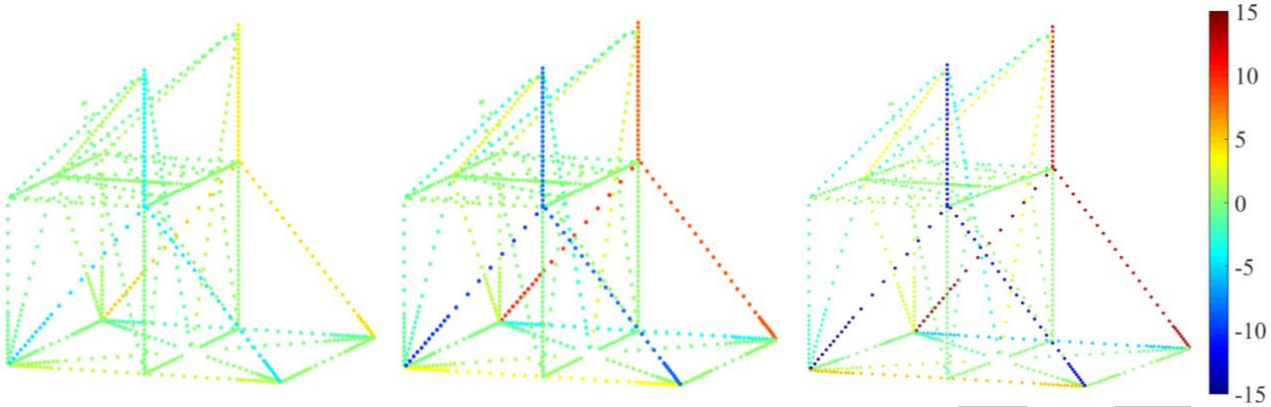

(a) $T = 5\ °C$ *(b)* $T = 10\ °C$ *(c)* $T = 15\ °C$

Figure 11: Weighted temperature for different uniform temperature distributions (5 – 10 – 15 [°C]) – φ_y *component.*

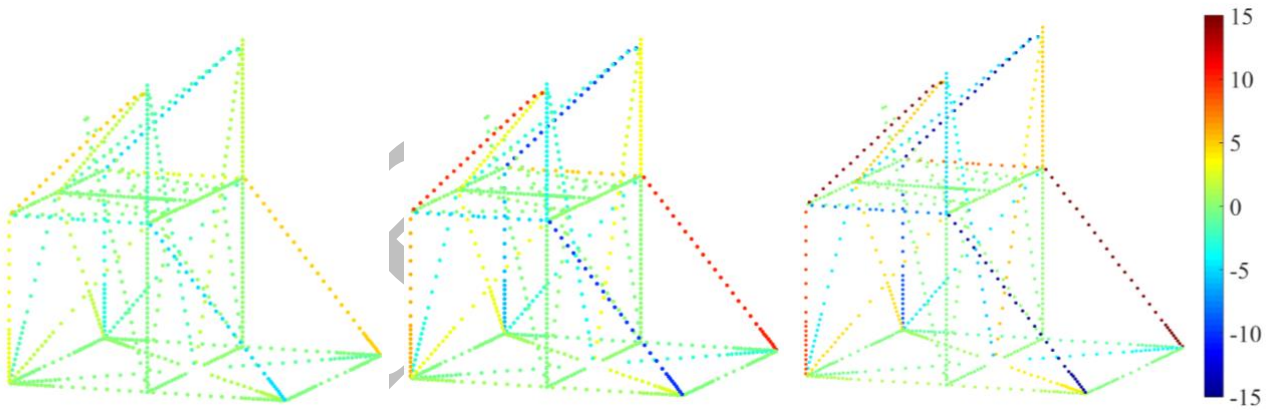

(a) $T = 5\ °C$ *(b)* $T = 10\ °C$ *(c)* $T = 15\ °C$

Figure 12: Weighted temperature for different uniform temperature distributions (5 – 10 – 15 [°C]) – φ_z *component.*

Uniform Temperature distribution		T=5°C	T=10°C	T=15°C
WTG for the rotation components	*x*-component	0.10194	0.20387	0.30581
	y-component	0.00046	0.00092	0.00138
	z-component	0.00659	0.01319	0.01978

Table 3: Weighted Thermal Gradient for all uniform temperature distributions analyzed (5 – 10 – 15 [°C]), referred to each rotation component.

4. Heat balance model

The aim of this section is to obtain an analytical model capable of simulating realistic thermal scenarios due to environmental conditions and estimating the effects on the antenna pointing error.

Heat can be transferred by means of conduction, convection and radiation. The simultaneous heat propagation by convection and radiation is called thermal adduction. Temperature variation of SRT's structural elements are inevitably produced by these thermal phenomena.

In addition, given the characteristics of our case it is possible to ignore conduction effects in long elements such as alidade trusses. For example, Figure 13 shows the rapid decrease of temperature in a 20m steel truss subjected to a thermal load of -3°C at one end with environmental temperature of 21°C. It can be seen that after almost one third of the span the truss temperature is almost constant, and it is similar to the environmental one. Thus, in the following we will ignore heat conduction among trusses that converge in the same node and will consider only convection and radiation.

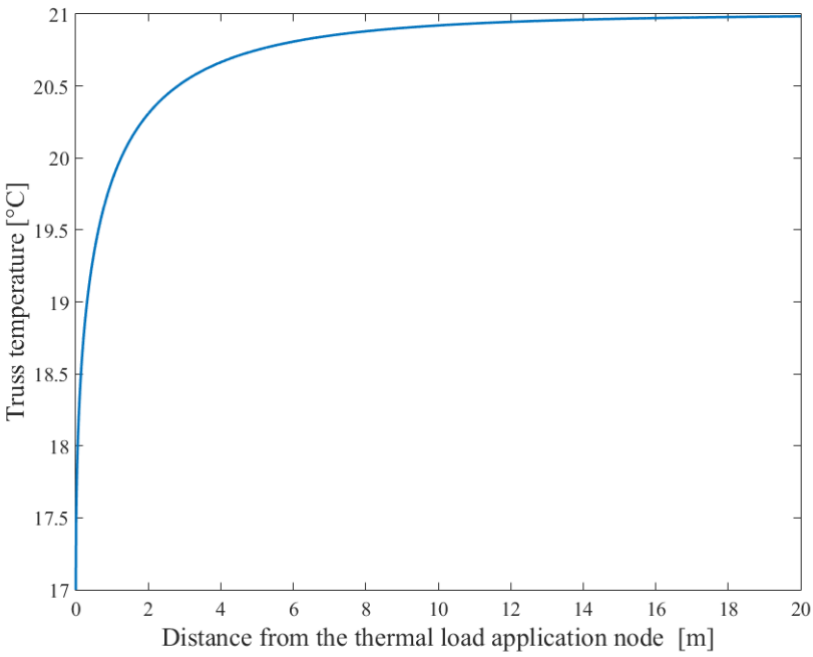

Figure13: Temperature distribution in alidade steel truss under conductivity thermal load.

When the radiative flux is incident on a surface, part of it is reflected. Therefore, the energy that leaves the surface consist in the algebraic sum of reflected radiation and emitted radiation. Instead, the non-reflected radiation energy penetrates the considered object and, crossing it, undergoes an attenuation. The part of it that crosses the object is called transmitted radiation, and the difference is called absorbed radiation.

For a given surface, the relevant reflection coefficient ρ, transmission coefficient τ, and absorption coefficient α, can be defined. However, most of solids are defined as opaque and they don't transmit thermal energy $\tau = 0$, but they only absorb it and reflect it, so that the remaining parameters are related by Equation (3)

$$\alpha + \rho = 1 \tag{3}$$

Considering short time intervals, it is possible to simplify the problem by assuming stationary conditions. Thus, the evaluation of the energy exchanged can be described through an energy balance on a control volume. There are examples of the use of this approach in the literature. In (Prado and Ferreira, 2005) the heat balance equation is used to calculate the surface temperature of roofs in Brazil for an estimate of albedo; in (Vox et al., 2016) the study of passive systems for the control of the thermal gain caused by sunlight is addressed; in (Höppe, 1993) the energy balance is used to describe in detail the environmental thermal effects on the human

311 body; (Bhumralkar, 1975) analyzes the energy exchange between the atmosphere and the soil under different
312 conditions of radiation influence by integrating the Rand two-level general circulation model.
313 If the considered surface is opaque, the heat balance equation is (Höppe, 1993):

314 $$\dot{Q} = A(ER + \rho G - G) \quad (4)$$

315 where $\dot{Q}$ is the net thermal power transferred from the surface A to the environment by radiation only; ER is
316 the thermal radiation emitted by the surface A which can be estimated through the Stefan-Boltzmann law for
317 real bodies (7):

318 $$ER = \varepsilon \sigma {T_p}^4 \quad (5)$$

319 where ε is the emissivity, σ is the Stefan-Boltzmann constant (8)

320 $$\sigma = 5{,}67\ 10^{-8} \left[\frac{W}{m^2 K^4}\right] \quad (6)$$

321 T_p is the surface A temperature, G is the solar radiation that strikes the same surface and ρG is the rate of
322 reflected solar radiation. If we take into account the convection effects:

323 $$\dot{Q}_c = A\, \dot{q}_c = A\, h_c\, (T_p - T_a) \quad (7)$$

324 where $\dot{q}_c$ denotes the convection flux between the surface A and the environment, h_c is the convection
325 coefficient between the same surface and the air, T_p is still the surface temperature and T_a is the environmental
326 temperature.

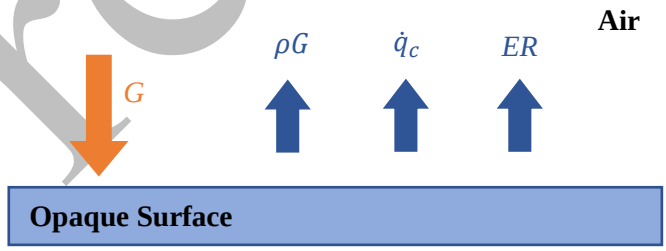

327 *Figure 14: considered terms in the energy balance.*

328

329 Expressing the terms indicated in Figure 14 and in Eq. (4) and Eq. (7) for a unit surface (i.e. A=1), yield Eq.
330 (8) and (9):

331 $$G = \rho G + \dot{q}_c + ER \quad (8)$$

332 $$G = \rho G + h_c \left(T_p - T_a\right) + \varepsilon \sigma {T_p}^4 \quad (9)$$

The reflection coefficient $\rho = (1 - \alpha)$ and the emissivity ε are expressed as a function of the surface conditions of the real body. For a white paint surface treatment as in the examined case, we can assume the following values for emissivity, absorption coefficient and reflection coefficient respectively: $\varepsilon = 0.88,\ \alpha = 0.14,\ \rho = 0.86$ (Kosky et al., 2013).

The convection coefficient is expressed in relation to the fluid where the thermal energy exchange takes place and to the stationary level of the fluid. If the fluid is not forced air, h_c assumes values between 2.5 and 25 $W\ /\ (m^2\ K)$ (Kosky et al., 2013); in this case it is set equal to 20 $W\ /\ (m^2 K)$.

Once the solar radiation *G* and the environmental temperature T_a have been identified, an algebraic equation of 4th degree in the unknown T_p is obtained, see Eq. (11), which can be solved by an iterative method.

5. Solar radiation analysis

The commercial Autodesk Revit software (Khemlani, 2004) was used to estimate the solar radiation that reaches each truss of SRT. The use of radiation simulation software allows to consider shadows and reflections generated by the radio telescope components and to study the effects of solar radiation incident to a surface characterized by a given percentage of obscuration.

A database of climatic information, included in the software, allows to obtain a hourly profile of environmental temperatures, i.e. an essential piece of information in the proposed analytical model.

The incident solar radiation (I_i) is evaluated through Eq. (10)

$$I_i = (I_b \cdot \cos\vartheta \cdot F_{sh}) + (I_d \cdot F_{sk}) + I_g \quad (10)$$

where I_b is the direct beam radiation which is measured perpendicular to the sun, ϑ is the angle where beam radiation affect the surface, F_{sh} represent the fraction of the surface currently in shadow from other surrounding geometry, I_d is the diffuse sky radiation, F_{sk} is the fraction of the diffuse sky visible in this instant from the surface and I_g is the radiation reflected from the ground. Furthermore, the average value of radiations that affects the four faces of the three-dimensional truss has been considered.

Please cite this document as: Attoli, A., Stochino, F., Buffa, F., Poppi, S., Serra, G., Sanna, G., & Cazzani, A. (2022). Sardinia Radio Telescope structural behavior under solar thermal load. In *Structures*, 39: 901-916. DOI: 10.1016/j.istruc.2022.03.065

At the end of the analysis, the total radiation relative to each daytime hour of the day is obtained; this piece of information is then used for the calculation of each element temperature using the model presented in Section 4. Figure 15 shows how the different position of the sun produces variable shading during the day. Obviously, an important role is played by the orientation and elevation angle of the antenna. The extent of solar radiation depends on all these aspects; it is clear how all this affects each antenna truss which will have a different temperature compared to the others in every situation. It is interesting to perform simulations for different configurations in terms of elevation, orientation and day of the year.

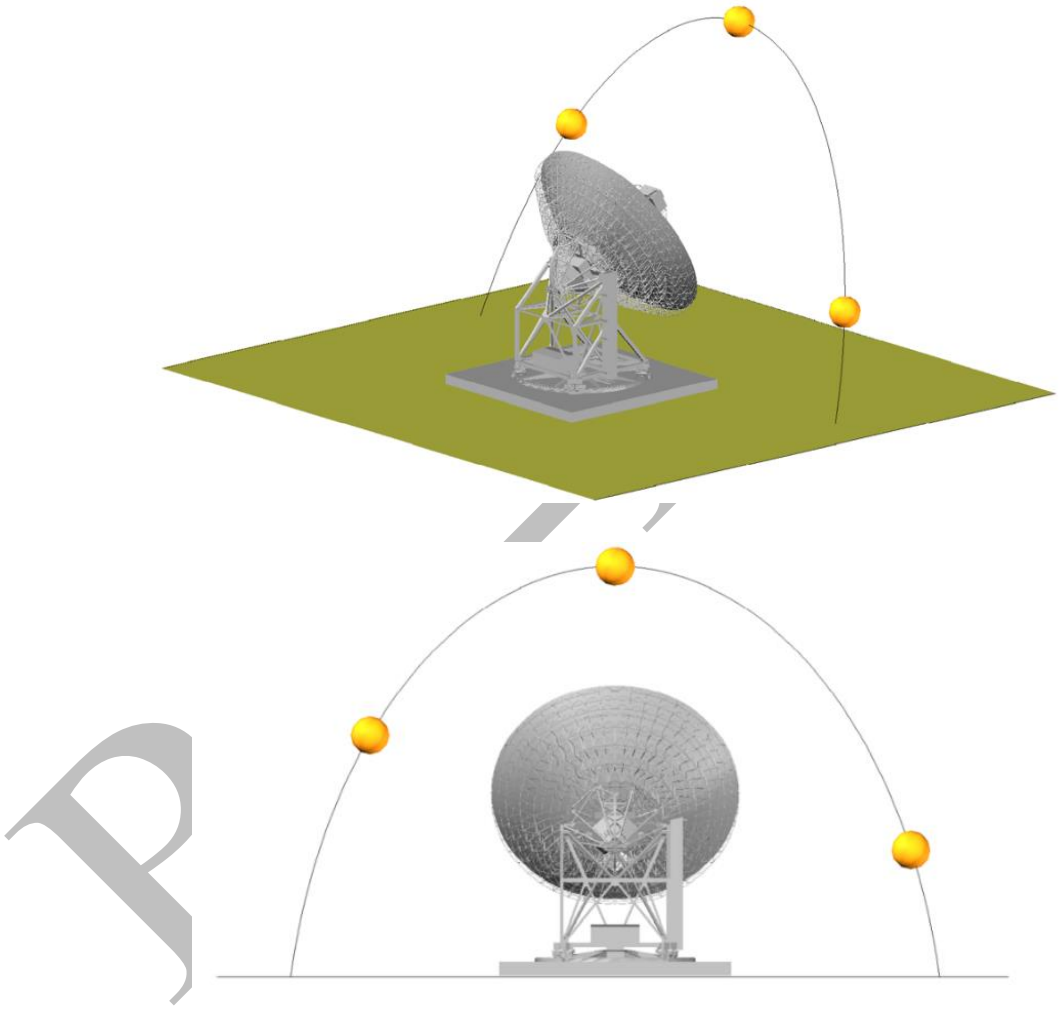

Figure 15: Different sun positions throughout the day, compared to Sardinia Radio Telescope

6. Calibration of heat balance equation parameters

In the preliminary phase, the values of the reflection coefficient ρ, absorption coefficient α and emissivity ε mentioned in the Section 4 were used. However, these are ideal values that may differ from the real ones. Indeed, the state of the coating with which the structure was treated shows imperfections due to normal atmospheric agents and oxidation typical of metal systems. These defects alter the ideal values of the parameters involved, influencing the temperature calculation.

In order to obtain realistic temperature values, a calibration of the reflection coefficient ρ and emissivity ε was carried out. This was made possible by using the data collected with a thermal imaging camera housed in a drone (see Figure 16).

The Flir Zenmuse XT thermal imaging camera was used for all investigations; it can operate in -25°C to +135°C scene range. When environmental conditions are ideal, this device provides an accuracy of ± 5°C.

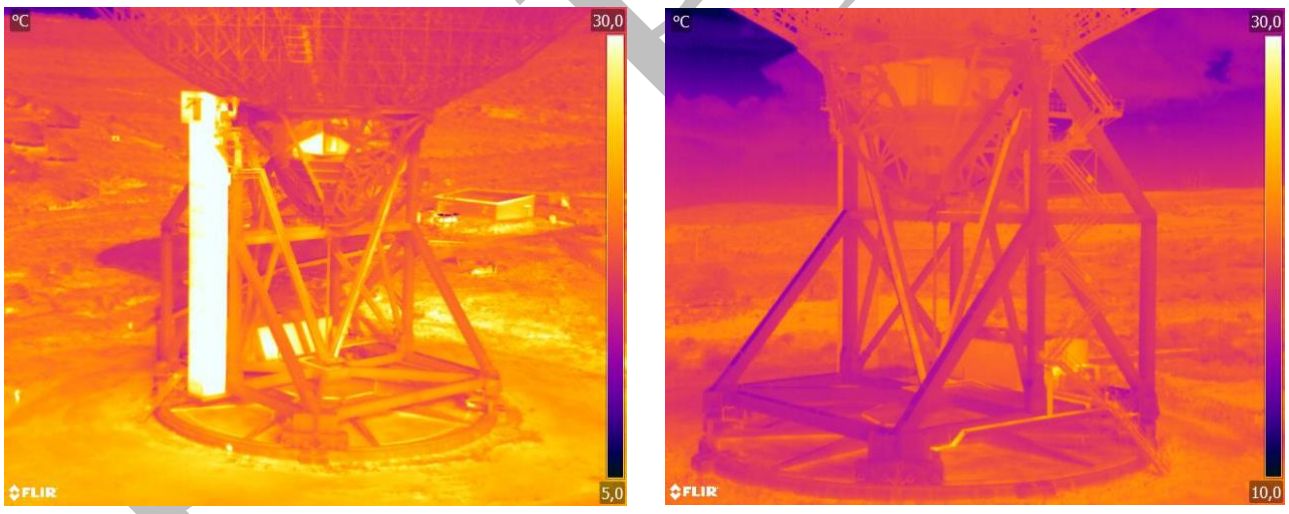

Figure 16: Thermal images captured by the drone.

Three surveys were carried out, in the daytime hours of September,11th 2020 , November, 19th 2020 and December, 31th 2020.

The images were taken on the four sides of the radio telescope in order to frame and characterize an adequate number of trusses which are useful for validating the model.

A local temperature measurement of the lower trusses (trusses that are located at eye level) was also performed, using an infrared thermometer in order to validate the temperatures measured with the thermal camera.

To estimate the real temperature of each truss, the average of the values of the visible 4 sides was evaluated. In addition, the temperature on each side of the truss was estimated as the average of the measurements in three points: in the center and at both ends (see Figure 17).

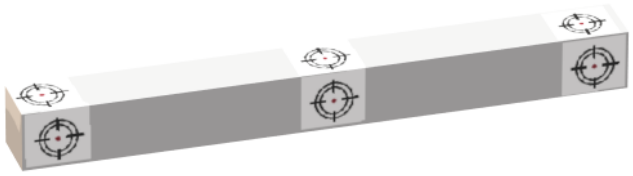

Figure 17: Point of elements where temperatures were measured.

The theoretical temperatures were calculated using the solar radiation values provided by the solar radiation model presented in Section 5 and the heat balance model presented in Section 4.

The values of the emissivity ε and reflection coefficient ρ were obtained with a least squares approach comparing the temperatures measured on site, which are adopted as benchmark, and the temperatures simulated with the analytical model. In this way, the following values for emissivity, reflection coefficient and absorption coefficient respectively were defined: $\varepsilon = 0.65$, $\rho = 0.60$, $\alpha = 0.40$.

Table 4 shows the comparison between measured and simulated temperatures for the trusses indicated in the thermal images (Figures 18-19) which are related to surveys carried out in two different campaigns: September, 11th 2020 on the left side and November, 19th 2020 on the right side.

Truss N°	Date	Local Time	Detected Truss Temperature [°C]	Simulated Truss Temperature [°C]	Date	Local Time	Detected Truss Temperature [°C]	Simulated Truss Temperature [°C]
8	11-set	10:00	16.0 – 17.0	17.2	19-nov	09:00	7.0 – 8.0	8.0
9	11-set	10:00	15.0 – 16.0	15.8	19-nov	09:00	7.0	7.5

44	11-set	10:00	17.0 - 18.0	17.9	19-nov	09:00	7.5 – 8.5	8.1

403 *Table 4: Simulation data for the two cases mentioned in the example.*

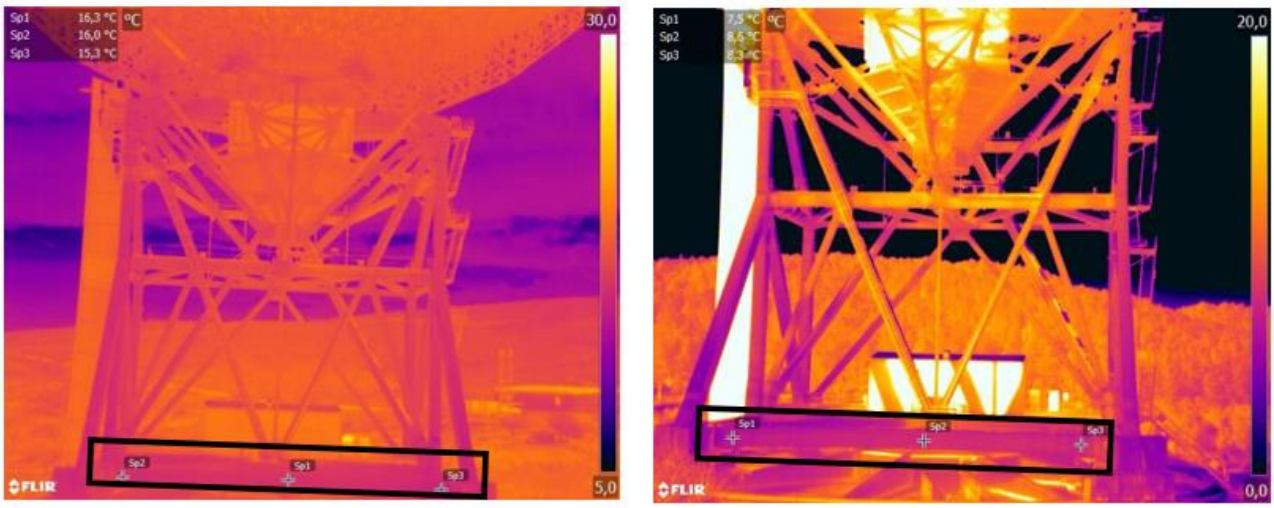

404

405 *Figure 18: Location of Sardinia Radio Telescope truss n°9 mentioned in the example.*

406

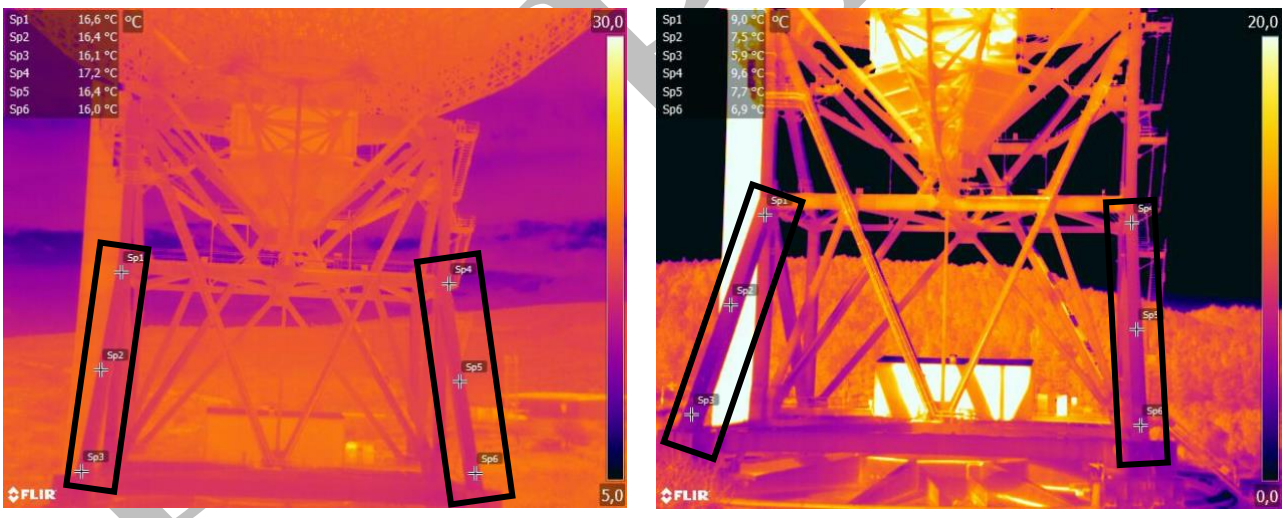

407

408 *Figure 19: Location of Sardinia Radio Telescope trusses n°8 (on the left side) and n°44 (on the right side),*

409 *mentioned in the example.*

410

411 Table 5 shows the difference between simulated temperatures and temperatures measured in three different

412 surveys for some of the 49 trusses of the alidade.

	11/09/2020 T_a=20°C		19/11/2020 T_a=15°C		31/12/2020 T_a=7°C	
Rod N°	Detected T [°C]	Simulated T [°C]	Detected T [°C]	Simulated T [°C]	Detected T [°C]	Simulated T [°C]
1	16.4	17.4	8.2	8.0	0.8	0.0
8	16.4	17.2	7.4	8.0	1.0	0.0
9	15.8	15.8	7.0	7.5	0.4	-0.3
10	15.7	15.8	7.7	7.5	-0.2	-0.3
12	15.7	16.0	7.8	7.5	-0.1	-0.3
28	16.4	16.0	7.0	7.4	0.6	-0.4
31	16.7	17.4	8.2	8.0	0.5	0.0
32	17.1	16.3	8.0	7.7	-0.3	-0.2
35	17.1	17.4	8.2	8.0	0.8	0.0
36	17.3	16.8	8.0	7.9	0.8	0.0
37	17.0	17.4	7.8	8.0	0.2	0.0
44	17.1	17.9	8.1	8.0	0.4	0.0
45	16.4	16.0	7.9	7.5	0.1	-0.3
46	16.4	16.0	7.9	7.5	0.1	-0.3

Table 5 : Comparison between simulated and detected temperature in three different surveys for some trusses of the Alidade.

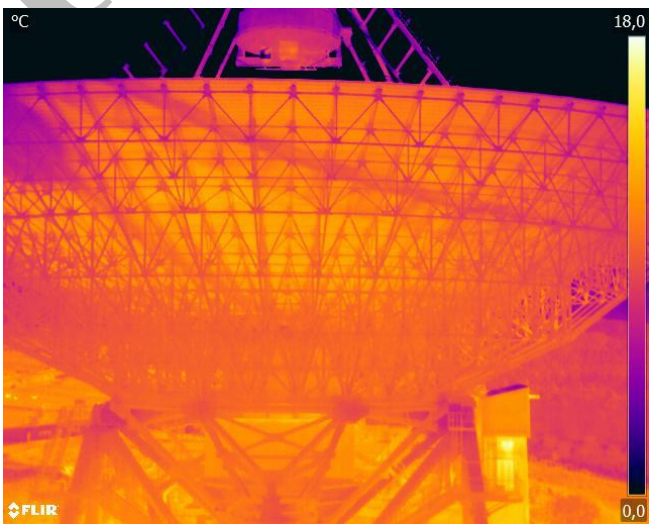

Please cite this document as: Attoli, A., Stochino, F., Buffa, F., Poppi, S., Serra, G., Sanna, G., & Cazzani, A. (2022). Sardinia Radio Telescope structural behavior under solar thermal load. In *Structures*, 39: 901-916. DOI: 10.1016/j.istruc.2022.03.065

Figure 20: Thermal images captured by the drone on November 2020

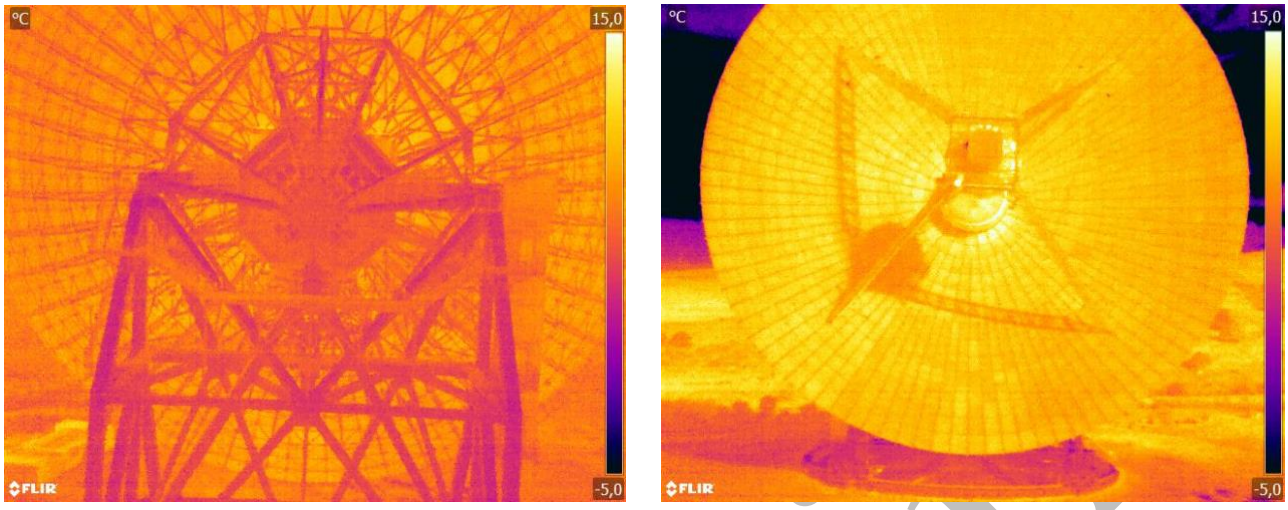

Figure 21: Thermal images captured by the drone on December 2020

Furthermore, in Figures 20-21 it is possible to see that the active surface panels can be significantly hotter than the alidade, BUS and Cradle trusses; the effect is due to the shading generated by the parabolic mirror.

Once the parameters were calibrated, each set of simulated temperatures corresponding to a given scenario can be applied to the finite element model for the calculation of the focus pointing error.

7. Numerical results.

Given the results of the sensitivity analysis described in Section 2, our attention was focused on the effects of irradiation on the alidade trusses and on how this affects the pointing vector of the radio telescope.

In particular, in four representative days of each season of the year (February 5th, May 5th, August 5th and November 5th) 9 simulations were performed: three elevation angles of the parabola, 90 deg, 60 deg and 30 deg, three orientation of the parabola in the North, East and South direction were considered.

The combinations have been chosen to represent most of the possible scenarios in which the Sardinia Radio Telescope operates, in order to represent its behavior in the four seasons. The simulations were developed

434 considering a reference local time (12:00) for all the analyzed cases. The values of Pointing Vector Rotations

435 (PVR) obtained for all the considered load scenarios are shown in Figures 22-24

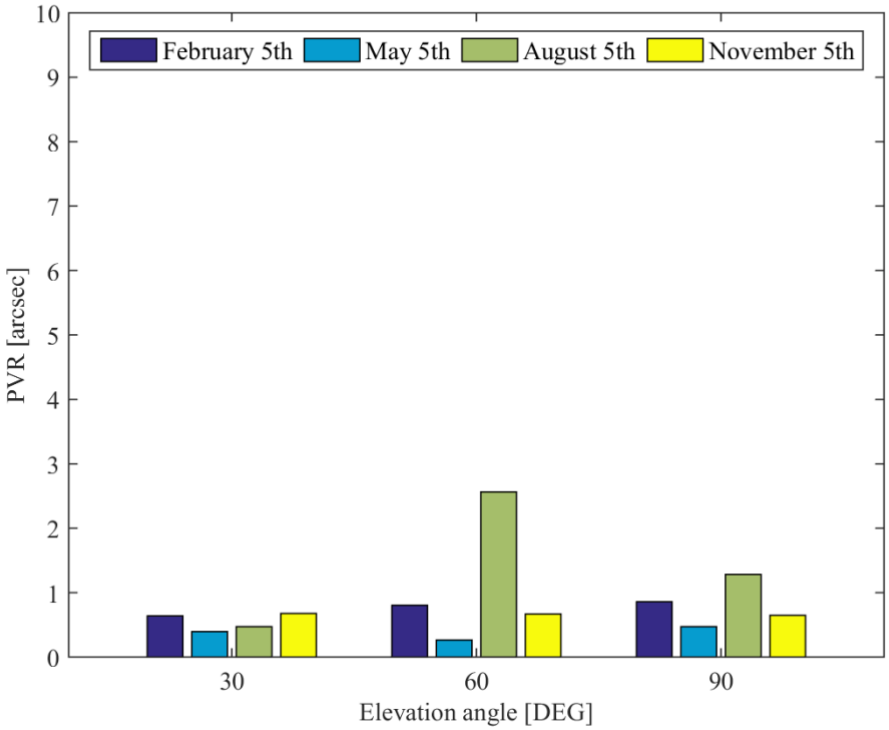

436

437 *Figure 22: Point Vector Rotation* (PVR) *for the 4 analyzed days. (Configuration with NORTH Orientation).*

438

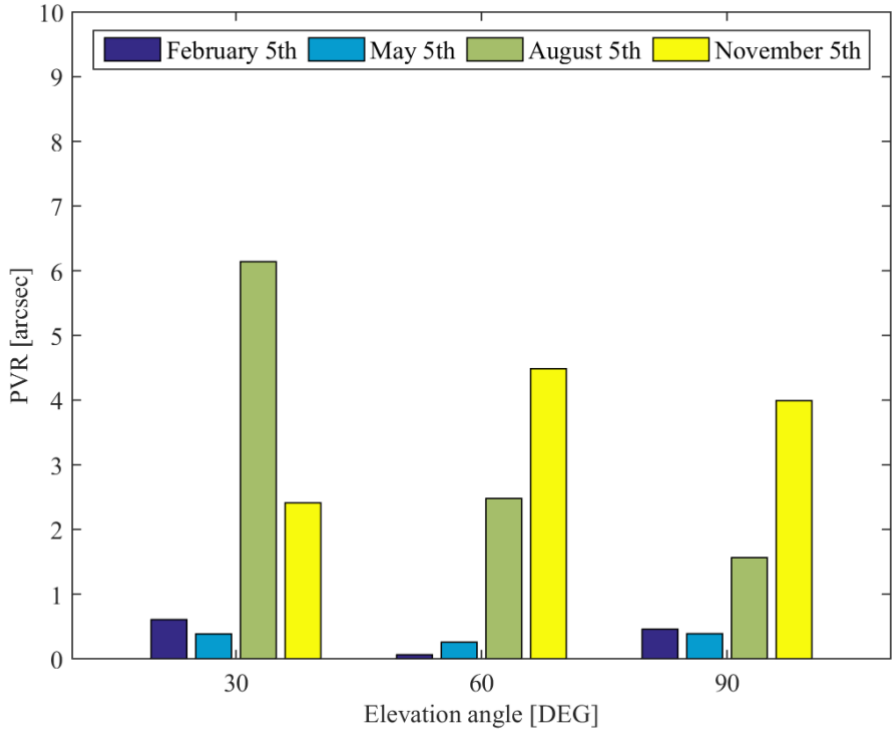

439

440 *Figure 23: Point Vector Rotation* (PVR) *for the 4 analyzed days. (Configuration with EAST Orientation).*

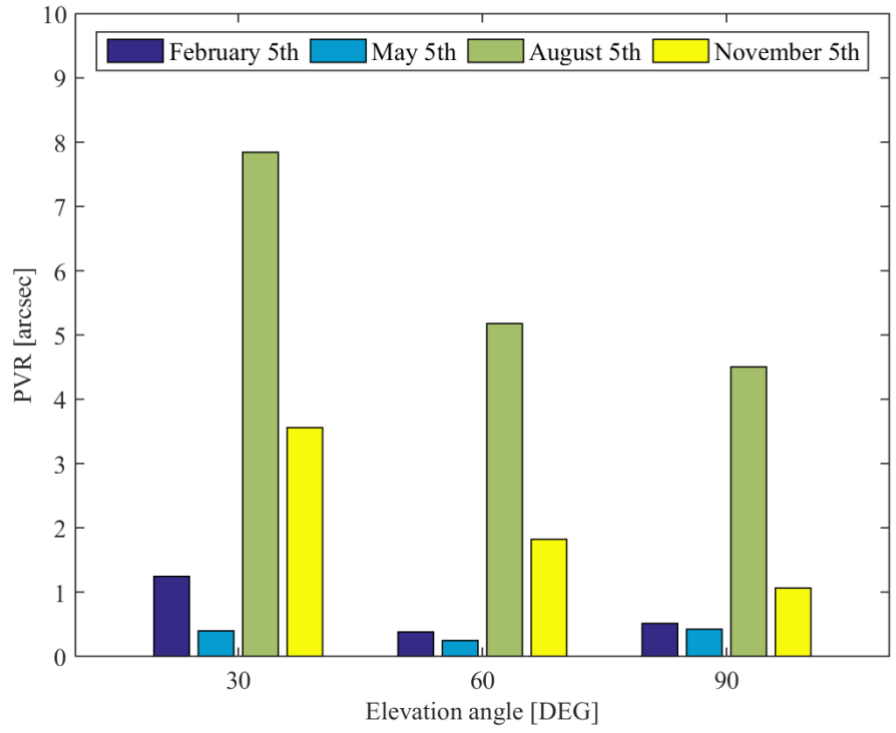

441

442 *Figure 24: Point Vector Rotation* (PVR) *for the 4 analyzed days. (Configuration with SOUTH Orientation).*

443

444 The diagrams show that thermal loads have an important influence on the SRT's structural behaviour, as it
445 affects its accuracy. It is also evident that the increase of environmental temperature during the year does not
446 inevitably produce an increase of the pointing error.

447 Table 6 presents the environmental and average truss temperatures for the South orientation.

448

449

SOUTH ORIENTATION				
Day	Environmental tempertaure [°C]	30 deg Elevation Average truss temperatures of the Alidade [°C]	60 deg Elevation Average truss temperatures of the Alidade [°C]	90 deg Elevation Average truss temperatures of the Alidade [°C]
February 5th	14	9.48	9.45	9.43
May 5th	18	11.59	11.58	11.57
August 5th	28	22.37	22.44	22.39
November 5th	13	6.46	6.37	6.38

450 *Table 6:Values of Environmental temperature and Average truss temperatures of the Alidade. (Configuration*
451 *with SOUTH Orientation).*

452

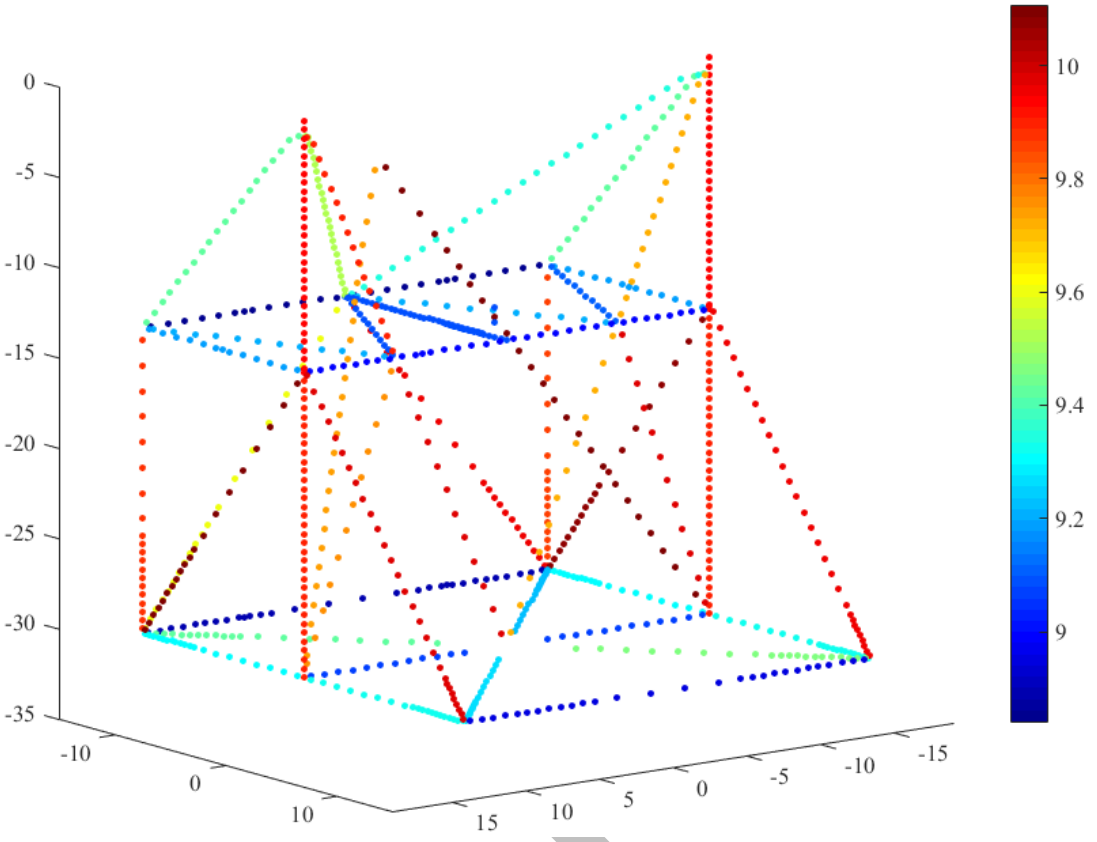

Figure 25: Distribution of temperatures in the Alidade trusses referring to the case of Elevation 60 deg with EST orientation for February 5th. [°C]

Average Temperature	9.46956
Standard deviation of temperatures	0.39612

Table 7: Statistical data for temperature distribution applied to the Alidade's trusses.

Pointing Vector Rotation Produced			
φ_x [arcsec]	φ_y [arcsec]	φ_z [arcsec]	PVR [arcsec]
-0.02692	-0.00026	-0.05578	0.06194

Table 8: Dataset of the Pointing Vector Rotation produced.

Figure 25 shows an example the distribution of temperatures in the Alidade trusses referring to the case of Elevation 60 deg with EST orientation for February 5th; the statistical parameters of the distribution are indicated in Table 7. Table 8 shows the values of the rotations produced by the thermal scenario applied to the FEM model; it can be seen that the rotation around the *z* rotation axis is of the same order of magnitude as the rotation around the *x*-axis. The lack of symmetry with respect to the *z*-*x* plane prevents φ_z rotations from cancel each other out.

	x-component **[°C]**	*y*-component **[°C]**	*z*-component **[°C]**
Absolute value of (WTG) for the rotation components	0.04416	0.00124	0.03897

Table 9: Order of magnitude of the Weighted Thermal Gradient for the rotation components of pointing vector.

Table 9, related to the above described example, shows how the Weighted Thermal Gradient (WTG) of x-rotation is of the same order of magnitude to the one obtained for z rotation.

Looking at the obtained results, no trend related to the variation of seasonal environmental temperatures can be defined. Indeed, the dominant aspect is the different irradiation caused by the geometric configuration of the entire antenna.

8. Discussions and Conclusions.

In this paper, the effects on the pointing error of SRT produced by solar radiation acting on its structural system have been studied. Through a sensitivity analysis it was possible to establish that the Alidade is the component of the radio telescope that produces greater pointing errors when subjected to a thermal load. Figure 26 highlights the most important trusses (n. 1, 2, 6, 7, 8, 14, 28, 31, 32, 36, 37, 44, 47, 48, see Figure 8), to evaluate the thermal load effects on pointing error.

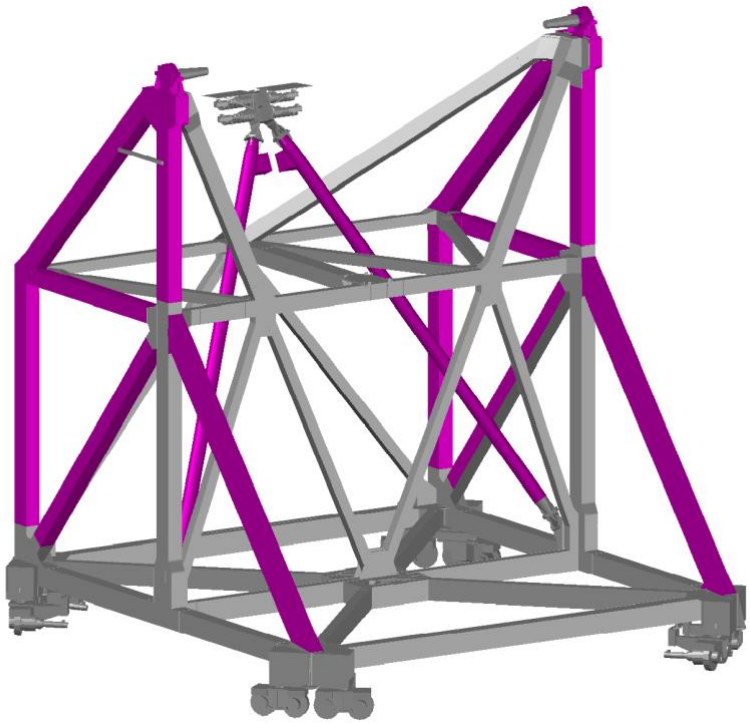

Figure 26: Alidade's trusses that produces greater pointing errors when subjected to a thermal load.

Then, an analytical model was used to estimate the temperature of the Alidade trusses, by means of solar radiation determined with a numerical model. Furthermore, the calibration of the analytical model parameters was performed by comparing the experimental data deriving from thermographic investigations performed on the entire antenna. Using Finite Element Analysis, the pointing error generated by each simulated thermal scenario was determined. Finally, the results obtained made it possible to better understand the structural behavior of the Sardinia Radio Telescope under simplified, but realistic thermal conditions.

Looking at the results for the South Orientation in Figure 24, it can be noted that the value of the Pointing Vector Rotation in November is higher than the corresponding value in May for each elevation angle, despite the average temperature of the trusses in spring is higher than that in autumn. The trend is not confirmed by the data referring to August, in which case both maximum temperature value and maximum PVR are found for this configuration (see Table 6). It is important to clarify that the average element temperatures obtained by the solar irradiation model (Revit software and analytical model) are an approximation that requires the use of the ANSYS FE model to evaluate the effects on the pointing vector error.

The phenomenon is therefore significantly influenced by the variable distribution of temperatures in the Alidade elements. The shading given by the position of the sun with respect to the antenna and the elevation of the parabola can result in a different irradiation of the trusses bringing them to uneven temperatures. In this case, since trusses in a symmetrical position with respect to the *z*-*y*-plane are subjected to different thermal load, the compensation of rotations around the *y* and *z* rotation axes due to the geometric symmetry of the Alidade is lost (as discussed in Section 3). For these reasons, unlike the case of uniform temperature distribution, φ_y and φ_z assume the same importance as φ_x, presenting the same order of magnitude.

When temperature distribution is not uniform, it is not possible to clearly delineate a trend for the total Pointing Vector Rotations because it is conditioned by the combined effect of:

- the value of WTG_x which depends on the temperature difference among trusses that generate opposite rotations around the *x*-axis;
- the values of WTG_y and WTG_z which depend on the temperature difference among the Alidade trusses located in a symmetrical position with respect to the *z*-*y*-plane; they increase φ_y and φ_z rotations respectively.

In conclusion, the pointing error is more influenced by the shading than by the seasonal variation of the solar radiation.

The need to continuously monitor the temperature of the trusses in order to forecast the pointing vector variation arises from this analysis. Through a metrological system it is possible to acquire temperatures from thermocouples distributed in optimal positions over the entire Alidade structure. In this way, the obtained data

519 can be processed in the finite element model for estimation, at any time, of the pointing error generated by
520 thermal conditions. Finally, this would allow to forecast the antenna pointing correction.
521

Please cite this document as: Attoli, A., Stochino, F., Buffa, F., Poppi, S., Serra, G., Sanna, G., & Cazzani, A. (2022). Sardinia Radio Telescope structural behavior under solar thermal load. In *Structures*, 39: 901-916. DOI: 10.1016/j.istruc.2022.03.065

Symbol	Description
μ	Density
E	Young's modulus
ν	Poisson's ratio
ψ	Expansion coefficient
PVR	Point Vector Rotation
φ_x	Rotations of the pointing vector around the *x*-axis.
φ_y	Rotations of the pointing vector around the *y*-axis.
φ_z	Rotations of the pointing vector around the *z*-axis.
IC	Influence Coefficient
WTG	Weighted Thermal Gradient
ρ	Reflection coefficient
τ	Transmission coefficient
α	Absorption coefficient
ε	Emissivity
$\dot{Q}$	Thermal power transferred by radiation
A	Reference surface
ER	Thermal radiation emitted by a surface
G	Solar radiation
σ	Stefan-Boltzmann constant
T_p	Surface temperature
T_a	Environmental temperature
$\dot{Q}_c$	Thermal power transferred by convection
$\dot{q}_c$	Convection flux between surface and environment

h_c	Convection coefficient
I_i	Incident solar radiation
I_b	Direct beam radiation
I_d	Diffuse sky radiation
I_g	Radiation reflected from the ground
ϑ	Angle where beam radiation affect a surface
F_{sh}	Fraction of surface currently in shadow from other surrounding geometry
F_{sk}	Fraction of the diffuse sky visible in this instant from a surface

Table 10: Symbols and acronyms

Bibliography

Ambrosini R., Grueff G., Morsiani M., Maccaferri G., Zacchiroli P., Orfei A., Analysis of the alidade temperature behaviour of the Medicina VLBI radiotelescope, *Astrophysics and Space Science*, 239, 247-258, 1996.

Bhumralkar C. M., Numerical experiments on the computation of ground surface temperature in an atmospheric general circulation model, *Journal of Applied Meteorology*, 14, 1246-1258, 1975.

Bolli P., Orlati A., Stringhetti L., Orfei A., Righini S., Ambrosini R., Bartolini M., Bortolotti C., Buffa F., Buttu M., Cattani A., D'Amico N., Deiana G., Fara A., Fiocchi F., Gaudiomonte F., Maccaferri A., Mariotti S., Marongiu P., Melis A., Migoni C., Morsiani M., Nanni M., Nasyr F., Pellizzoni A., Pisanu T., Poloni M., Poppi S., Porceddu I., Prandoni I., Roda J., Roma M., Scalambra A., Serra G., Trois A., Valente G., Vargiu G. P., Zacchiroli G., Sardinia Radio Telescope: General description, technical commissioning and first light. *Journal of Astronomical Instrumentation*, 4(03n04), 1550008, 2015.

Buffa F., Causin A., Cazzani A., Poppi S., Sanna G., Solci M., Stochino F., Turco E., The Sardinia Radio Telescope: A comparison between close-range photogrammetry and finite element models, *Mathematics and Mechanics of Solids*, 22, 1005-1026, 2015.

Chen D., Xu W., Qian H., Sun J., Li J., Effects of non-uniform temperature on closure construction of spatial truss structure, *Journal of Building Engineering*, 32, 101532, 2020.

Chen D., Xu W., Qian H., Wang H., Thermal behavior of beam string structure: Experimental study and numerical analysis, *Journal of Building Engineering*, 40, 102724, 2021.

Drozdzol K., CFD thermal analysis of a three-layer chimney used in residential buildings, *Journal of Building Engineering*, 44, 102665, 2021.

Fu L., B. Ling Q. B., Geng X. G., Wang J. Q., Jiang Y. B., Yu L. F., Zhang Y. F., The alidade temperature behaviour of TM65m antenna and its effects on pointing accuracy, *Advances in Optical and Mechanical Technologies for Telescopes and Instrumentation II*, *Proc. SPIE 9912*, 99124J, 2016.

548 Greve A., Bremer M., Peñalver J., Raffin P., Morris D., Improvement of the IRAM 30-m Telescope from
549 temperature measurements and Finite-Element calculations, *IEEE Transactions on Antennas and*
550 *Propagation*, 53, 851-860, 2005.
551 Govoni F., Bolli P., Buffa F., Caito L., Carretti E., Comoretto G., Fierro D., Melis A., Murgia M., Navarrini
552 A:, Orfei A., Orlati A., Pisanu T., Poppi S., Possenti A., Attoli A., Becciani U., Belli C., Carboni G., Caria
553 T., Cattani, A., Concu, R., Cresci L., Fara A., Fiocchi F., Gaudiomonte F., Ladu A., Maccaferri A., Mariotti
554 S., Marongiu P., Migoni C., Molinari E., Morisani M., Nesti R., Olmi L., Porceddu I., Righini S., Ortu P.,
555 Palmas S., Pili M., Poddighe A., Poloni M., Roda J., Scalambra A., Schillirò F., Schirru L., Serra G.,
556 Smareglia R., Vargiu G.P., Vitello F., The high-frequency upgrade of the Sardinia Radio Telescope. In
557 XXXIVth General Assembly and Scientific Symposium of the International Union of Radio Science (URSI
558 GASS) (pp. 1-4). IEEE, 2021.
559 Höppe P. R., Heat balance modelling, *Experientia*, 49, 741-746, 1993.
560 Khemlani, L. Autodesk Revit: implementation in practice. White paper, Autodesk, 2004.
561 Kosky P., Balmer R., Keat W., Wise G., Exploring Engineering 3rd edition, *Academic Press*, 2013.
562 Li L., Lin W., Zhang T., Liu X., On-site measurement of thermal environment and heat transfer analysis in a
563 curling arena, *Journal of Building Engineering*, 34, 101691, 2021.
564 Losi G., Bonzanini A., Aquino A., Poesio P., Analysis of thermal comfort in a football stadium designed for
565 hot and humid climates by CFD, *Journal of Building Engineering*, 33, 101599, 2021.
566 Pisanu T., Buffa F., Poppi S., Marongiu P., Serra G., Vargiu G. P., Concu R., The SRT inclinometer for
567 monitoring the rail and the thermal gradient effects on the alidade structure, *Ground-based and Airborne*
568 *Telescopes V*, *Proc. SPIE 9145*, 91454R, 2014.
569 Prado R. T. A., Ferreira F. L. Measurement of albedo and analysis of its influence the surface temperature of
570 building roof materials, *Energy and Buildings*, 37, 295-300, 2005.
571 Stochino F., Cazzani A., Poppi S., Turco E., Sardinia Radio Telescope finite element model updating by means
572 of photogrammetric measurements, *Mathematics and Mechanics of Solids*, 22, 885-901, 2015.

Please cite this document as: Attoli, A., Stochino, F., Buffa, F., Poppi, S., Serra, G., Sanna, G., & Cazzani, A. (2022). Sardinia Radio Telescope structural behavior under solar thermal load. In *Structures*, 39: 901-916. DOI: 10.1016/j.istruc.2022.03.065

573 Stolarski, T., Nakasone, Y., Yoshimoto, S. Engineering analysis with ANSYS software. Butterworth-
574 Heinemann, 2018.
575 Süss, M., Koch, D., Paluszek, H. The sardinia radio telescope (SRT) optical alignment. In Ground-based and
576 Airborne Telescopes IV (Vol. 8444, p. 84442G). International Society for Optics and Photonics (2012,
577 September).
578 Ukita N., Ezawa H., Ikenoue B., Saito M., Thermal and wind effects on the azimuth axis tilt of the ASTE 10-
579 m Antenna, *Publications of the National Astronomical Observatory of Japan*, 10, 25-33, 2007.
580 Vox G., Maneta A., Schettini E., Evaluation of the radiometric properties of roofing materials for livestock
581 buildings and their effect on the surface temperature, *Biosystems Engineering*, 144, 26-37, 2016.
582 Wang M., Ou T., Xin Z., Wang D., Zhang Y., Mechanical behavior and fatigue failure analysis of standing
583 seam aluminum alloy roof system under temperature effect, *Journal of Building Engineering*, 44, 103001,
584 2021.
585 Zhao Y., Du J., Xu Q., Bao H., Real-time monitoring of the position and orientation of a radio telescope sub-
586 reflector with fiber bragg grating sensors, *Sensors*, 19, 619, 2019.

Please cite this document as: Attoli, A., Stochino, F., Buffa, F., Poppi, S., Serra, G., Sanna, G., & Cazzani, A. (2022). Sardinia Radio Telescope structural behavior under solar thermal load. In *Structures*, 39: 901-916. DOI: 10.1016/j.istruc.2022.03.065